NANO · MICRO small
www.small-journal.com

# Solution-Controlled Conformational Switching of an Anchored Wireframe DNA Nanostructure

*Ian T. Hoffecker, Sijie Chen, Andreas Gådin, Alessandro Bosco, Ana I. Teixeira, and Björn Högberg**

**Self-assembled DNA origami nanostructures have a high degree of programmable spatial control that enables nanoscale molecular manipulations. A surface-tethered, flexible DNA nanomesh is reported herein which spontaneously undergoes sharp, dynamic conformational transitions under physiological conditions. The transitions occur between two major macrostates: a spread state dominated by the interaction between the DNA nanomesh and the BSA/streptavidin surface and a surface-avoiding contracted state. Due to a slow rate of stochastic transition events on the order of tens of minutes, the dynamic conformations of individual structures can be detected in situ with DNA PAINT microscopy. Time series localization data with automated imaging processing to track the dynamically changing radial distribution of structural markers are combined. Conformational distributions of tethered structures in buffers with elevated pH exhibit a calcium-dependent domination of the spread state. This is likely due to electrostatic interactions between the structures and immobilized surface proteins (BSA and streptavidin). An interaction is observed in solution under similar buffer conditions with dynamic light scattering. Exchanging between solutions that promote one or the other state leads to in situ sample-wide transitions between the states. The technique herein can be a useful tool for dynamic control and observation of nanoscale interactions and spatial relationships.**

## 1. Introduction

Since the introduction of DNA nanotechnology[1] and more recently the DNA origami technique,[2] increasingly complex structures have been demonstrated based on the programmed self-assembly of DNA molecules through elementary base pairing (e.g., refs. [3–8]). Next generation therapeutics and biological research increasingly depend on dynamic manipulation of nanoscale structures such as proteins and nucleic acids, and DNA nanostructures are a strong candidate for executing such manipulation due to the high level of structural sophistication currently achievable. Controlling the shape and conformations of DNA nanostructures has been explored through a variety of means, the majority of which fall within two general categories: bond cleavage-based and entropy-driven strategies.

Cleavage-based strategies involve the breakage of covalent bonds in the polynucleotide sequence resulting in major changes at the structural level, e.g., via enzymatic cleavage,[6,9,10] photocatalytic cleavage,[11] or reduction of disulfide bonds.[11,12] Due to the greater morphological fidelity and predictability of static structures, rigidity is often a desired characteristic of nanostructures.[13] However, polynucleotide flexibility, exhibiting a greater conformational entropy, can be harnessed for various applications such as in the minimization of ligand–receptor enthalpy by enabling unstrained coupling. Such a tradeoff has been demonstrated between binding entropy and thermal stability.[14] A class of state-switching strategies based on conformational mobility-mediated annealing includes a variety of toehold-mediated strand displacement approaches.[15–20] Such strategies hold in common the exploitation of polynucleotide flexibility to explore a continuum of microstates in order to reach distinct macrostates. This approach has been used to manipulate the structure of large DNA origami nanostructures, for example, a box-structure with an opening and closing lid actuated by the introduction of oligonucleotide "keys" that displace securing strands enabling passive opening along a basic hinge.[21] Another instance is a 3D tetrahedron that underwent discrete reversible conformational changes in the presence of strand-displacing signal molecules.[22] A disadvantage to these approaches is the generation of waste strands and nontrivial reversibility.

In this work, we adopt pH and cation concentration as control parameters of local interaction potentials[23] to constrain the conformation space of DNA nanomeshes tethered to a

Dr. I. T. Hoffecker, Dr. S. Chen, A. Gådin, Dr. A. Bosco, Prof. A. I. Teixeira, Prof. B. Högberg
Biomaterials
Department of Medical Biochemistry and Biophysics
Karolinska Institutet
Solnvägen 9, 171 65 Solna, Sweden
E-mail: bjorn.hogberg@ki.se
Dr. S. Chen
Ming Wai Lau Centre for Reparative Medicine
Karolinska Institutet
Hong Kong Science Park
Hong Kong
Hong Kong Special Administrative Region
China
The ORCID identification number(s) for the author(s) of this article can be found under https://doi.org/10.1002/smll.201803628.

DOI: 10.1002/smll.201803628

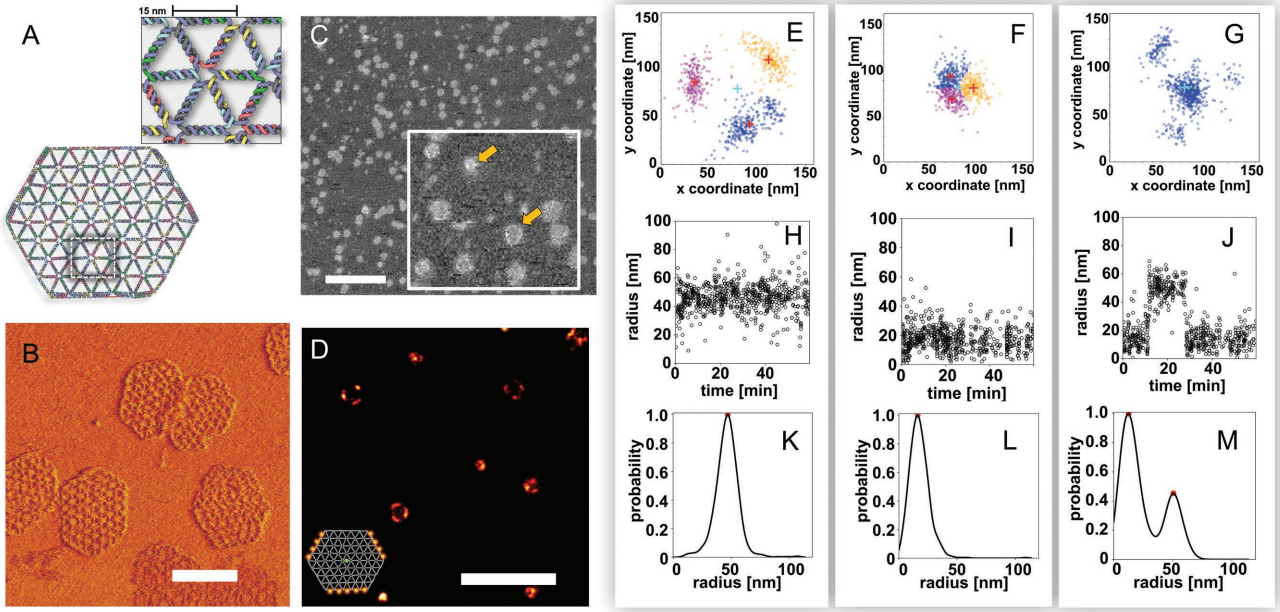


**Figure 1.** Analysis of individual structures tethered to biotinylated-BSA/streptavidin surface via a single central anchor strand. A) vHelix design of a hexagon wireframe nanomesh. B) AFM image of hexagonal nanostructures on mica. Scale = 100 nm. C) Hexagon nanostructures anchored via a central biotinylated oligo on a surface of streptavidin, coupled to adsorbed biotinylated BSA and imaged with AFM in QI-mode. Inset at higher magnification revealed small and large structures suggesting a distribution of structural conformations. Scale (bar and inset side length) = 1 µm. D) A representative region of a DNA PAINT image of centrally anchored structures. Imager strand docking sites are located on three edges (bottom left diagram). Structures exhibit different degrees of spreadness, appreciable by the internal separations of labeled edges. Scale = 500 nm. E) Scatter plot of localizations corresponding to a spread structure with symmetry detected using k-means clustering (3 color scheme). Red crosses denote cluster centroids. Blue cross denotes the average of the 3 cluster centroids and the assigned central point of the structure. F) Scatter plot of PAINT localizations from a contracted structure. G) Scatter plot of PAINT localizations for a dynamic structure with three lobes surrounding a 4th central lobe, algorithmically identified by a failure to maintain symmetry with three clusters. H) Time series plot of radii extending out from the central point of (E). I) Time series plot of radii extending out from the spread structure central point from (F). J) Time series plot of radii from (G). K) Radial probability density function (PDF) of the structure from (E) and (H) generated using kernel density estimation. L) Radial PDF of the structure from (F) and (I) generated using kernel density estimation, showing a peak located at smaller radius compared to (K). M) Radial PDF of the structure from (E) and (H) generated using kernel density estimation with a distinct bimodal characteristic.

BSA/streptavidin-coated glass surface. Recently we presented a framework for automated, computer-aided design and self-assembly of complex 2D nanostructures from arbitrary wireframe designs that are stable in a variety of solutions including magnesium-free solutions and PBS.[24] The structures, which are formed from a mesh of single helices, are more flexible than the tightly packed helices of traditional DNA origami, resulting in a continuum of conformational states. We found that structures were either pinned to the surface in a spread and open conformation or alternatively in a closed or contracted state depending on whether the solution conditions were of high calcium and high pH or relatively low calcium or low pH, respectively, and that this action is likely mediated by electrostatic interactions between structures and surface bound BSA/streptavidin.

## 2. Results

We designed hexagonal, planar DNA nanostructures with single-helix thickness and dimensions of 104 nm on two hexagonal axes and 140 nm on the third hexagonal axis using the vHelix framework[7,24,25] (Figure S1, Supporting Information). Atomic force microscopy (AFM) images of structures (**Figure 1**A,B) give a characteristic appearance of flatness, guided by adherence to underlying mica surface.

Structures immobilized to a glass surface of adsorbed biotinylated BSA and streptavidin via a central biotinylated staple exhibited structures adopting a range of sizes when imaged with AFM in quantitative imaging (QI) mode to handle high topographic noise (Figure 1C). To better characterize this conformational distribution, we used DNA PAINT (point accumulation for imaging in nanoscale topography),[26,27] a variant of single molecule localization microscopy. In this method, accumulation of stochastic blinking events are achieved from the transient binding and unbinding of small 9-base oligonucleotides conjugated to fluorophores as they enter a limited 100–200 nm range of a TIRF evanescent wave. Docking sites for PAINT were placed redundantly along the peripheral edges of three sides of the hexagon (Figure 1D inset). We initially examined structures in the presence of PAINT buffer B,[27] an aqueous tris-buffered solution of pH 8 containing $1 \times 10^{-3}$ M EDTA and $10 \times 10^{-3}$ M $MgCl_2$. Reconstructed images (Figure 1D) revealed a diverse range of structure sizes, consistent with the AFM findings, clearly indicating the morphological distinctions between conformations. We

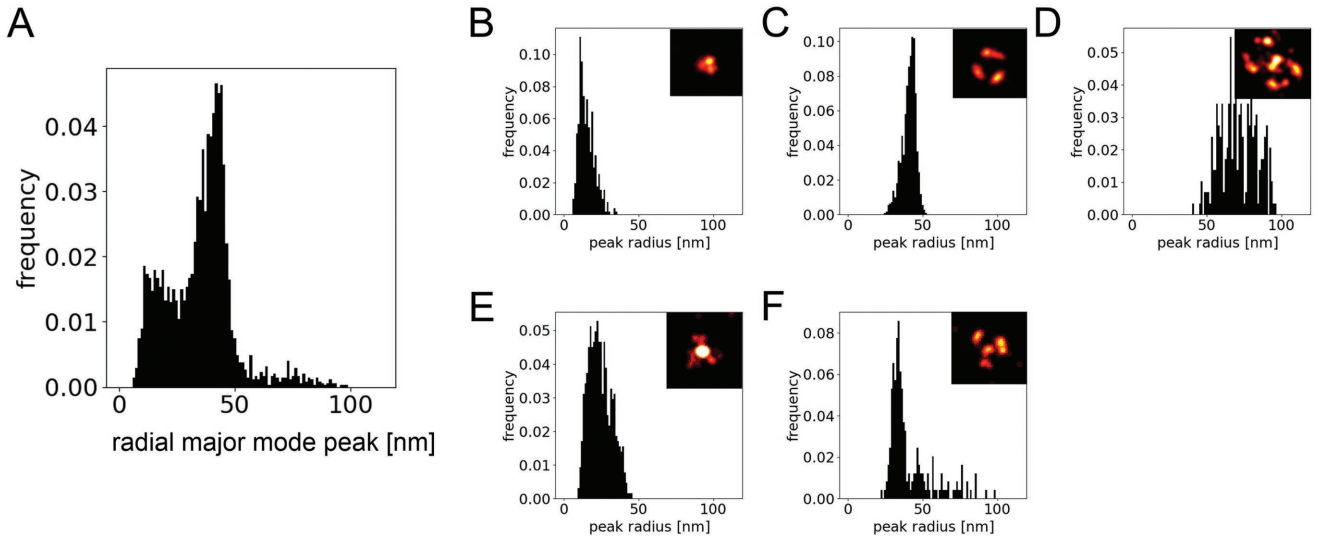


**Figure 2.** Population level analysis of structures imaged with DNA PAINT. A) Distribution of the dominant radial peaks for all structures imaged in buffer (B). B–F) Histograms of the major mode data from radial probability distributions of various classes identified from clustering of radial variables and corresponding to those denoted in the plot from (B). Representative examples of a structure of each class are shown in upper right corner of each panel. B) Distribution of radial peaks for a class of structures exhibiting contracted conformation. C) Distribution of radial peaks for a class of structures exhibiting spread conformation. D) Distribution of radial peaks for a class of structures sharing the trait of dimerism. E) Distribution of radial peaks for a class of structures exhibiting dynamic contracted/spread conformation where the majority of time was spent in contracted conformation. F) Distribution of radial peaks for a class of structures exhibiting dynamic contracted/spread conformation where the majority of time was spent in spread conformation thus shifting the distribution to the right relative to (E).

wrote an image processing script to extract localization data of individual structures. Scatter plots of the localizations for representative structural variants are shown in Figure 1E–G, with spread structures such as that plotted in Figure 1E, identified by their characteristic three sides of clustered DNA PAINT docking sites alternating with unlabeled sides. Numerous structures exhibited a collapsed or contracted conformation (Figure 1F). Finally, a fraction of structures shared features of spread and contracted structures, an apparent overlapping of the two motifs (Figure 1G). We performed further processing to extract radial distributions, first by using spatial clustering (see the Experimental Section) to identify the three labeled edges, taking the average of the assigned cluster centers as the center of the structure, and then computing the radius from this central point out to each localization, i.e., the projection of the structure radius onto the imaging plane. Localization radii as a function of time, corresponding to the structures in Figure 1E–G are shown in Figures 1H–J, respectively. The radii in spread structures such as that in Figure 1E remain consistently high throughout the duration of the experiment (mean radial peak 50 nm ± 10 s.d. in the case of Figure 1H compared to $r = 53.5$ nm and $r = 72$ nm shortest and largest dimensions, respectively, by design). While the radii of contracted structures are consistently low (11 nm ± 8 s.d. in the case of Figure 1I), the third category of "dynamic" structures exhibit marked shifts in the radial distribution over time that appear to be discrete step transitions from low to high or high to low radial values. A representative structure shown in Figure 1J was initially in the contracted conformation (mean radius 15 nm ± 8 s.d.), and when 9.4 min of imaging time had elapsed, it underwent a sharp transition to spread conformation. In the interval between 9.4 and 25.5 min, the structure had a mean radius of 38 nm ± 6 s.d., after which it transitioned sharply back to a contracted state for the remaining duration of the experiment with mean radius of 11 nm ± 6 s.d.

We determined the radii of the dominant state by extracting Gaussian kernel density estimates of the radial probability density functions (PDF) (Figure 1K–M) (the major mode of the radial PDF), a more precise metric for radius that can accommodate cases when multiple radial peaks or skewed distributions would distort the mean radius. We examined the distribution of these peak radii the population of structures to understand how conformations were distributed within the time interval. **Figure 2**A shows the overall distribution of radius peaks for the sample depicted partially in Figure 1D. The distribution appears to have multiple overlapping modes, so we used multidimensional clustering to separate the population into distinct classes according to their structural features, namely their average radius, the radius variance, and the integer number of modes detected in the kernel density estimated radial PDFs (**Figure 3**B). Classes emerge with qualitatively distinct structural morphologies and corresponding prevalence in the sample radial distribution. Structures with a positively skewed radial distribution peaking close to zero relative to the overall population could be identified as the contracted class (Figure 2B) with an average radial peak of 15 nm ± 5 s.d. whereas a class of spread structures had an average radial peak of 40 nm ± 5 s.d. (Figure 2C). The theoretical radial limit of correctly folded structures is ≈60 nm, and a significant peak of the overall distribution spanning the range 50–100 nm represents a population of dimeric structures which we can appreciate visually from reconstructed images within the class (Figure 2D). Two dynamic (bimodal) classes emerged whose major mode corresponded either to the radius of the contracted state

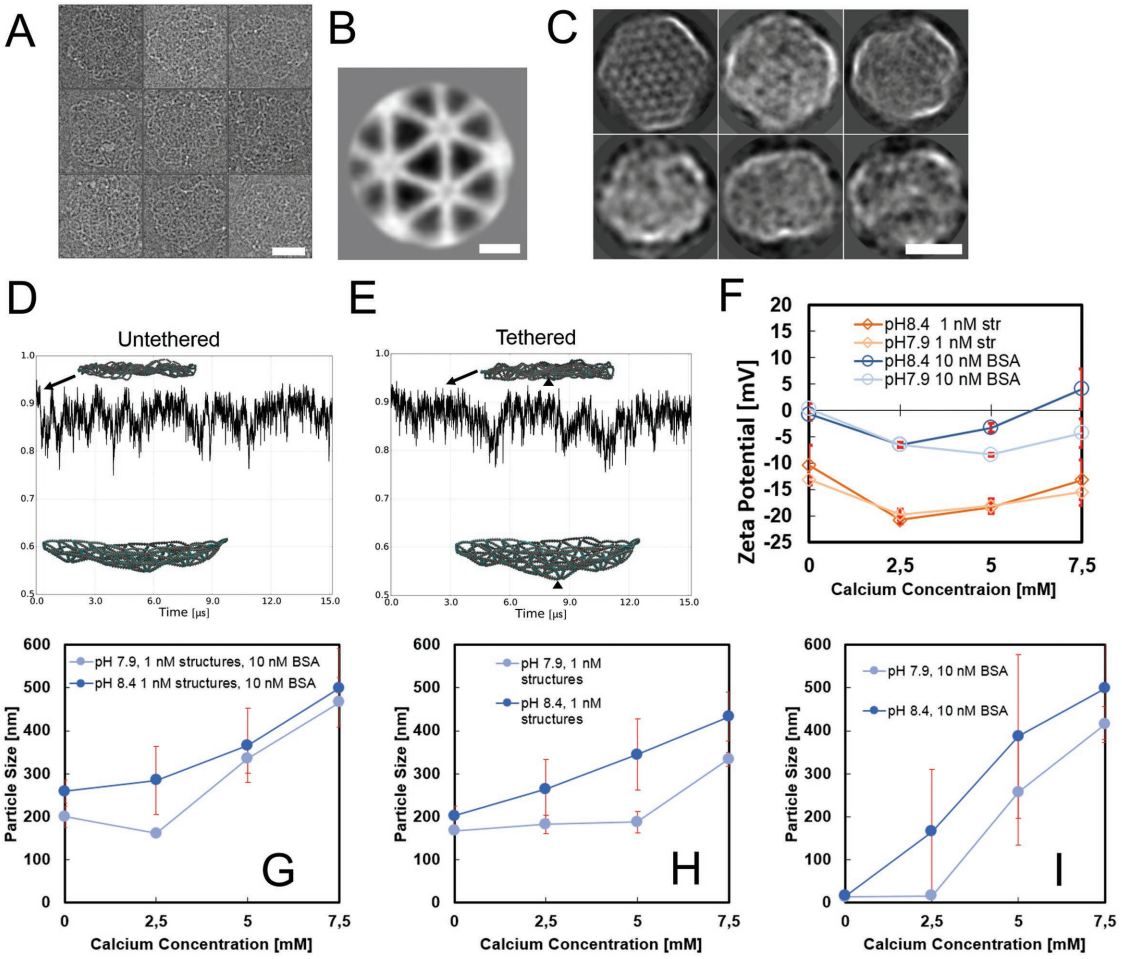


**Figure 3.** Characterization of untethered structures in solution. A) Cryo-EM images of single hexagonal nanostructures. Scale = 50 nm. B) Class average of cryo-EM images with limited 20 nm reconstruction radius. The repetitive hexagonal lattice and pseudodegeneracy (sequences differ but lattice junctions are structurally similar) enabled high resolution reconstruction of the lattice with single-helix resolution. Scale = 10 nm. C) Class averages of cryo-EM images. Structures were suspended in 1× PBS. Although not directly tethered to the surface, some topographical guidance may occur with structures close to the ice–air interface whereas others are less spatially confined. Scale = 50 nm. D) Coarse grained simulation of untethered structure in free solution for 15 μs, initialized with an unstrained spread state. E) Coarse grained simulation of an anchored structure for 15 μs, initialized with an unstrained spread state. F) Independently acquired zeta potential measurements of either BSA or structures in blood buffers of either high (8.4) or low (7.9) pH plotted as a function of calcium concentration. G–I) Dynamic light scattering size intensity peak measurements indicating aggregation at relative increased pH and calcium ion concentrations. Error bars indicate standard error of the mean $n = 3$ replicates of independently prepared solutions. G) A combination of $1 \times 10^{-9}$ M structures with $10 \times 10^{-9}$ M BSA for pH 7.9 (dotted line) and pH 8.4 (solid line) solutions of varied calcium ion concentration. H) $10 \times 10^{-9}$ M BSA only for pH 7.9 (dotted line) and pH 8.4 (solid line) solutions of varied calcium ion concentration. I) $1 \times 10^{-9}$ M structures only for pH 7.9 (dotted line) and pH 8.4 (solid line) solutions of varied calcium ion concentration.

(Figure 2E) or to the spread state (Figure 2F) with their minor modes respectively corresponding to the spread and contracted states, i.e., indicating the state in which the majority of the time interval was spent.

Examination of structures in solution did not lead to conformational variety of the kind observed when tethered to streptavidin/BSA surfaces. Cryo electron microscopy (cryo-EM) imaging was used to examine the structures without any topographic guidance, and structures suspended freely could be seen adopting a diverse range of conformations, with representative images shown in Figure 3A. Class averaging of 40 nm diameter portions of multiple single particles highlights the hexagonal junction in agreement with the design, with the repeated lattice allowing for degenerate alignment of regions smaller than a single particle and high single-helix resolution (Figure 3B). Larger diameter class averages (130 nm) revealed a range of spread structural classes (Figure 3C) suggesting a continuum of spread conformations and flexibility but not the distinct structural states such as the drastically reduced radial dimension of contracted structures tethered onto the streptavidin/BSA surfaces. We used coarse grained simulations of untethered (Figure 3D) and tethered (Figure 3E) structures under similar ionic conditions as those of cryo-EM and the tethered experiments anticipating that the confinement due to tethering would lead to a cupped conformation due to entropic constraints on the structure's conformational space (i.e., from a spherical range of conformations to a hemisphere with a single planar face). However simulations indicate that only

limited entropic cupping occurs as a result of tethering—corresponding to several of the cryo-EM classes that exhibit a limited inward cupping without any major collapse. Measuring the radial projection onto the tethering plane (analogously to radii gathered from the isometric view of DNA PAINT), we obtained a radial measurement for simulated structures at steady state as a fraction of the radius at initial conditions. Median values differed between untethered and tethered by less than 1% (Figure 3F) suggesting that the observed conformational changes could not be explained by an entropic spring effect alone, but rather that surface interactions are likely responsible for the states observed with BSA/streptavidin-immobilized structures.

In order to explore electrostatic interactions between the structures and the surface, we examined the particle size distributions and zeta potentials of structures in solutions with BSA. $10 \times 10^{-9}$ M BSA suspended in PAINT buffer B exhibited a size peak of 12. ± 2 nm s.e., $1 \times 10^{-9}$ M structures alone a peak of 154. ± 9 nm s.e., and a combination of the two ($1 \times 10^{-9}$ M structures and $10 \times 10^{-9}$ M BSA) a bimodal distribution with one peak at 159 ± 40 nm and another at 10.0 ± 0.3 nm s.e. Zeta potentials, measured for the individual components only, for $10 \times 10^{-9}$ M BSA and $1 \times 10^{-9}$ M structures were –8.0 ± 0.4 mV s.e. and –5.8 ± 1.6 mV s.e., respectively. We systematically modulated solvent attributes pH and ionic concentration to manipulate the interaction potentials of structures and BSA. Structures suspended in a buffer mimicking the contents of blood plasma (blood buffer, Table S1, Supporting Information) exhibit similarly negative zeta potential values (Figure 3F, orange) at both a low pH in the range 7–7.9, at higher pH of 8.4, and over a range of different calcium ion concentrations (with $2.5 \times 10^{-3}$ M being the physiological concentration). By contrast, we observed that the zeta potential values for BSA with calcium concentrations above $2.5 \times 10^{-3}$ M diverge, taking on different values depending on which pH was used (Figure 3F, blue). In the range of $5 \times 10^{-3}$ to $7.5 \times 10^{-3}$ M [$Ca^{2+}$], a charge inversion occurred for the high pH case. We did a DLS-based screen of pH values for blood buffer ($2.5 \times 10^{-3}$ M Calcium) with $1 \times 10^{-9}$ M structures and $1 \times 10^{-9}$ M BSA and observed an apparent phase transition with aggregation occurring above pH 8.2 and stabile suspension below that value (Figure S8, Supporting Information). DLS size measurements in the two buffers show the size of the peak corresponding to structures occurring in the range 100–400 nm to depend on the calcium ion concentration for a mixture of structures and BSA, with the modulus of this dependence greater in the high pH case (Figure 3G). The aggregative effect was also observed for BSA and structures independently (Figure 3H,I).

In addition to a panel of other buffer conditions (Figure S9, Supporting Information), we examined tethered structures with PAINT in the nonaggregative low pH/low calcium conditions and the high pH/high calcium aggregative conditions. Blood buffer with pH in the range between 8.2 and 8.4 promoted a peak radial distribution dominated by the spread conformation (**Figure 4**A) and the radial peak distribution showed that the majority of structures have a peak radius in the high >25 nm range (Figure 4B). When the sample was prepared with buffer of pH between 7 and 7.9 a population-wide shift to predominantly contracted conformation (Figure 4C) was observed, with radial peak distribution in the low (<25 nm) range (Figure 4D), similar in appearance to the radial sub-population of contracted structures from Figure 2B. Finally, blood buffer with 2× the $2.5 \times 10^{-3}$ M physiological calcium concentration ($5 \times 10^{-3}$ M) led to the highest observed radii, all together supporting a pH dependent, cation-mediated interaction between structures and the adsorbed protein layer causing spread conformations and a steric electrostatic repulsion causing contracted conformations.

We constructed an on-stage fluidic injection system to perform in situ exchange of imaging solution in between PAINT rounds in order to examine a single field under alternating conditions and observed that structures could be dynamically switched to spread state by imaging first in pH 7.9 blood buffer followed then by pH 8.4 blood buffer (Figure 4F). PAINT dynamic analysis of the radii of each localization, with structure centers identified postreconstruction, binned (5 s), and averaged across the whole sample provide an average radial profile of the sample throughout the exchanges (Figure 4G) which shows a step response to alternating solutions introduced at 10, 20, and 30 min, demonstrating reversibility of the conformational change as well as controllability albeit with an apparent lag going from step 2 to step 3.

## 3. Discussion

Wireframe DNA nanostructures are structurally flexible compared to classical DNA origami formed from packed helices. With more structural degrees of freedom, the structures are able to explore a broader range of conformational microstates. However our previous investigations of such structures have not indicated a general tendency for the qualitative morphological transitions that we observed by DNA PAINT analysis.[24] The existence of a portion of the population that exhibited dynamic behavior, i.e., those that changed conformations during the duration of experiments, plus the possibility to immobilize structures consistently spread with peripherally placed biotin anchors rule out conformational determination during self-assembly of the structures.

The cryo-EM images showed a basically uniform conformational distribution in solution compared to that observed on surfaces with AFM and DNA PAINT, with only a continuum of spread and semispread structures with no collapsed or morphologically distinct structures. We explored the possibility that entropic tethering alone might be enough to induce a cupped-conformation by restricting degrees of freedom, i.e., reducing the total space of conformations to only those with a tethered center and on one side of a fixed plane. Coarse-grained simulations of this configuration revealed however that the structures are rigid enough at this size scale to be spread out, in line with our previous work investigating the structural determinants of wireframe nanostructure conformational consistency.[24]

It is more likely that intermolecular interactions in the composite surface system are responsible for the unique conformational transitions. Separate zeta potential measurements of structures and BSA in imaging buffer yielded negative values implying that under these conditions, the two particle types should exhibit a repulsive electrostatic interaction.

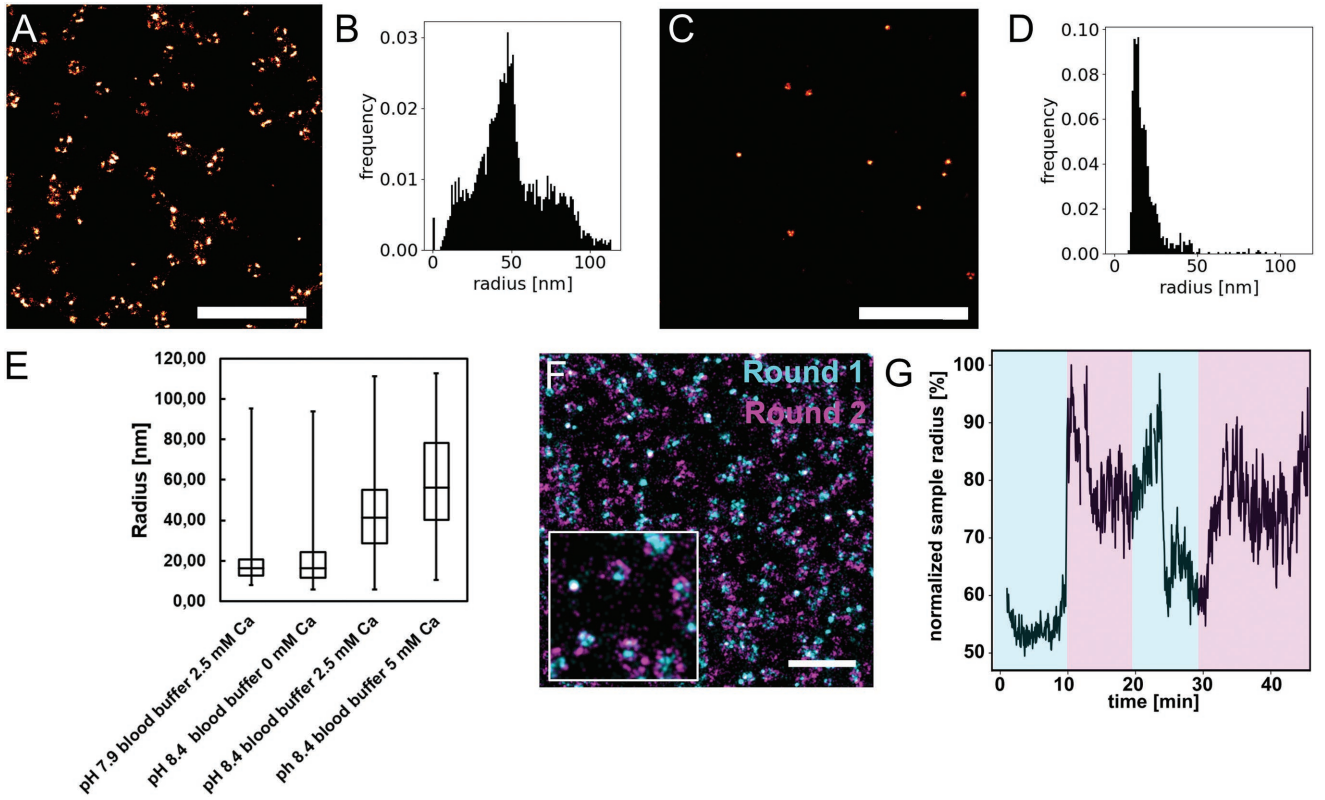


**Figure 4.** Control of hexagonal DNA nanostructure conformations via modulation of solution parameters. A) DNA PAINT reconstructed image for structures anchored and imaged in blood plasma-like buffer at pH of 8.4 exhibiting nearly universal spread conformation. Scale = 1 µm. B) Distribution of radial peaks of structures in pH 8.4 blood plasma-like buffer. C) Structures anchored and imaged in blood plasma-like buffer at pH 7.9 exhibiting nearly universal contracted conformation. D) Distribution of radial peaks of structures in pH 7.9 blood plasma-like buffer. E) Box and whisker plot comparison of the distributions of radial peaks of structures imaged in buffer conditions of varied pH and calcium content exhibiting diverging conformations. F) In situ switching from contracted (cyan) to spread (magenta) by exchanging imaging buffer, going from pH 7.9 to pH 8.4 blood plasma-like buffer. Scale = 1 µm. G) Radii of localizations averaged across sample plotted as a function of time with timed injections of blood buffer imager solutions: 0 min: pH 7.9; 10 min pH 8.4; 20 min pH 7.9; and 30 min pH 8.4.

While BSA isoelectric point occurs near pH 5.7, above which it should exhibit negative charge of increasing magnitude, zeta potential is determined by electric double layer and hence increases in available calcium and calcium binding capacity of BSA should push the particle zeta potential toward more positive values. Other studies have reported that albumin binds calcium at multiple locations and with a positive dependence on pH,[28] and the charge inversion observed at high pH and high calcium is likely to reflect this interaction. The divergence of BSAs zeta potential values in buffers with $>2.5 \times 10^{-3}$ M calcium levels and charge inversion occurring between $5 \times 10^{-3}$ and $7 \times 10^{-3}$ M in contrast to the relatively stable zeta potential values of structures under the same conditions means that the interaction would become attractive under these conditions. We observed this shift from repulsion to attraction and its dependence on pH and calcium via the size distribution shift in DLS measurements. Due to the resolution limit of DLS and the formation of BSA aggregations at calcium concentrations $\geq 5 \times 10^{-3}$ M that enter the size range of structures (100–400 nm) creates a confounding factor preventing a positive determination of BSA-structure aggregates in this range. Taken together, the results implicate surface protein–DNA interaction and ionic and pH modulation of electrostatic charges as the primary mechanism driving the attractive spread conformation and conversely a repulsive surface-avoiding closed conformation when both protein and structures are negatively charged.

## 4. Conclusion

To conclude, the conformational dependence on pH and calcium concentration and the correspondence to the diverging size and charge distributions of BSA under increasingly aggregative conditions indicates to us that these can be used as control parameters to manipulate surface interactions between surface and structure. One hurdle with this theory comes when attempting to resolve the contrast between the sharp discontinuities observed in radial time series plots with the apparently smooth continuous increase in zeta potential and DLS particle size, however such dramatic phase transitions are in agreement with similar phenomena observed for calcium-ion dependent condensation of polyelectrolytes and DNA and attributed to a propagation of local interactions or zipper-effect followed by collective stability due to multivalent affinity.[29] The use of such noncovalent interactions enables reversible control of the structures via tuning solution parameters, and we expect this feature

to be a useful principle for the dynamic control of nanoscale distances as a variety of strategies for incorporating biomolecules into DNA nanostructures implies that this platform could be adopted to control nanoscale distances and interactions between a variety of molecules of interest.

## 5. Experimental Section

*Design and Preparation of DNA Nanostructures*: Synthetic unmodified DNA oligonucleotide staples were purchased from Integrated DNA Technologies Inc. with purification by standard desalting and suspended in nuclease free water at $100 \times 10^{-6}$ M concentration, and oligonucleotide staples with a terminal biotin modification were ordered with HPLC purification. DNA nanostructures were designed using Maya and vHelix[7] (Figure S1, Supporting Information) and produced by assembling a mixture containing $10 \times 10^{-9}$ M M13mp18 (p7249) ssDNA scaffold and staple strand solution ($50 \times 10^{-9}$ M each) in 1× PBS (sequences listed in Supporting Information). Solutions were folded by placing them in a heating ramp beginning with rapid heat denaturation at 80 °C for 5 min and then cool from 80 to 60 °C over a 20 min interval, and finally cooled from 60 to 24 °C over a 14 h interval. Structures were purified by centrifugal filtration to remove staple strands using 100 kDa MWCO. 0.5 mL capacity Amicon spin columns (Millipore) with 1× PBS wash buffer at 14 000 rcf twice for 2 min each, discarding flow-through after each round. Structures were tested for folding quality before and after purification with a 2% agarose gel, 90 V, 2 h, in ice cold water, in 1× TBE buffer containing $10 \times 10^{-3}$ M $MgCl_2$ (Figure S2, Supporting Information). The concentration of nanostructures after purification and concentration was typically $5 \times 10^{-9}$ to $10 \times 10^{-9}$ M. Design considerations are discussed in further detail in Table S3 of the Supporting Information.

*Acquisition of DNA PAINT Localization Data of Anchored DNA Nanostructures*: DNA PAINT experiments were carried out according to the protocol described by Jungmann and co-workers.[27,30] Modified oligonucleotide imager strands (Sequence: 5′-CTAGATGTAT-atto 550 dye) were purchased from Integrated DNA Technologies Inc. Chambers for anchoring the nanostructures were assembled using microscope slide glass (VWR) that was cleaned first with acetone and propanol and then used as a base, attaching two parallel strips of double-sided Scotch tape and bridging the two strips with coverglass (no. 1 thickness, 18 × 18 mm) for a final chamber volume of 10 µL and dimensions $18 \times 5.5 \times 0.1$ mm. 1 mg $mL^{-1}$ biotinylated BSA (29130B, Thermo Fisher Scientific) solution in PAINT Buffer A ($10 \times 10^{-3}$ Tris-HCl, $100 \times 10^{-3}$ M NaCli, 0.05% Tween 20, pH 7.5) was injected (10 µL) into the chamber and incubated at room temperature for 2 min to allow adsorption to the glass surface and then washed out by exchanging the chamber with Buffer A (150 µL) by using an absorbent tissue wipe to withdraw waste solution. 0.5 mg $mL^{-1}$ streptavidin (21122, Thermo Fisher Scientific) suspended in Buffer A was then injected (10 µL) into the chamber and incubated for 2 min to allow the coupling of streptavidin to the layer of biotin BSA. The chamber was then washed again with Buffer A (150 µL) and then exchanged with sample buffer: PAINT Buffer B ($5 \times 10^{-3}$ M Tris-HCl, $10 \times 10^{-3}$ M $MgCl_2$, $1 \times 10^{-3}$ M EDTA, 0.05% Tween 20, pH 8), 1× PBS, TE-$Mg^{2+}$ Buffer, or blood buffer according to experimental conditions). DNA nanostructures with biotinylated oligonucleotide protruding sites (either in central scheme shown in Figure 2B or peripheral scheme shown in Figure S3, Supporting Information) suspended at $1 \times 10^{-9}$ M concentration in sample buffer were then injected (10 µL) into the chamber and incubated for 2 min to allow biotin anchors to attach to the layer of streptavidin on the surface. The chamber was then washed with sample buffer (150 µL). Imaging buffer containing oxygen scavengers PCA (40× stock prepared with 154 mg/10 mL $H_2O$ with 1 M NaOH added incrementally to dissolve PCA) and PCD (100× stock prepared with $50 \times 10^{-3}$ M KCl, $1 \times 10^{-3}$ M EDTA, $100 \times 10^{-3}$ M Tris-HCl, 50% glycerol, and PCD 0.7 mg $mL^{-1}$)[31] and Trolox (100× stock prepared by first dissolving 100 mg Trolox into 430 µL of ethanol, 3.2 mL of $H_2O$, and adding 1 M NaOH incrementally until dissolved) plus imaging strands ($10 \times 10^{-9}$ M) was then injected into the chamber (10 µL). The chamber was then sealed on four sides with epoxy adhesive. Samples were imaged using TIRF microscopy on a Nikon T7 with 1.49 NA CFI Plan Apo TIRF 100× Oil objective, Chroma ZET 561 emission and excitation filters, iLAS2 circular TIRF module, Andor iXon Ultra 888 EMCCD with 1024 × 1024 sensor size (13 µm pixel size). Timelapses were acquired with micromanager software to detect of stochastic binding events using 300 ms frames, 12 000 frames, 10 MHz readout rate. Localizations were detected using the Gaussian fitting algorithm and software platform Picasso from Jungmann and co-workers[27] with a 10 000 photon per localization threshold and stage drift correction and exported to .hdf files as lists of coordinate data.

*Image Reconstruction and Processing of DNA PAINT Localization Data*: Image reconstruction from localization coordinate data and further processing was carried out using custom code written in Python. Reconstruction of images from coordinates was accomplished by generating a 2D histogram of localization coordinates with the number of pixels determined by the square of the product of the original image length (256 px) with the subpixel resolution factor, which was 40 in all cases. Final values in each pixel were then normalized to a 256 value scale for visualization. Structures were identified algorithmically from reconstructed images by applying a Gaussian blur followed by Otsu thresholding to form continuous blobs. Blob coordinates ±35 pixel square boxes were cropped out to obtain reconstructed images of individual structures, the subset of localizations corresponding to the region containing each structure, time stamps of each localization, and photon counts of each localization that had been recorded with Picasso software. Radial data were computed for each structure by estimating first the center of each structure using k-means clustering (k = three clusters) on the localization data of each individual structure to identify the three lobes of clustered localizations resulting from the arrays of PAINT docking sites packed closely together on three sides of the structure. Structure centers were then computed as the average of the three cluster centroids. In cases where cluster yielded asymmetric or ambiguous results, the localization centroid was used as the center point, for example, in the case of dynamic structures with four lobes (three peripheral and one central). Radii were then computed as the distance from the center points out to each localization. Radial PDFs were estimated from radial data using Gaussian kernel density estimation with bandwidth selection according to Scott's rule. Note that kernel density estimation results in systematic over-smoothing and bias with multimodal distributions, thus dynamic structures with multimodal PDFs tended to have major modes detected closer to the center of the distribution. Time series plots of the radii of localizations throughout the course of an experiment for each structure were also generated by matching the timestamps of localizations with their associated radial data. Photon counts were plotted versus radial and time data to verify that there is no correlation between photon counts or double localization events with the observed conformation transitions (Figure S4, Supporting Information). Multivariate clustering was performed using k-means (k = 10) and structure variables: radius average, radius variance, and number of modes detected in the kernel density-estimated radial PDFs. Images were grouped according to class and visualized as montages (Figure S5, Supporting Information) and distributions were plotted for each class.

*Cryo-EM Imaging of DNA Nanostructures*: Structures were imaged in a Talos Arctica cryo-EM (FEI Company) at the Swedish Cryo-EM national facility located at Sci-Life Lab in Stockholm. Structures for imaging were prepared by folding them in PBS and concentrated in 100 kDa Amicon spin columns to 500 Grids were prepared using holey carbon 2/2 200 mesh, 120 s glow discharge at 25 mA, 2 s blot time, 1 s drain time, blot force 0, at 22 °C, 100% humidity. The exposure settings used were 9 $e^-$ $Å^{-1}$ $s^{-1}$ (4 s exposure, 36 $e^-$ total dose), 22 frames, 1.64 $e^-$ per frame, pixel size 3.25, 45 000× magnification, filament voltage 200 V, amplitude contrast 0.1, C2 aperture 70 µm, objective aperture 70 µm, C2 lens 46.061%. Contrast transfer functions were estimated with the CTFFind package and Scipion and then exported into Relion-2.0. Structures were gathered via manual particle picking and extracted.

2D classification was performed with 50 classes with mask diameters of 1300 Å in the case of whole structures and 600 Å in the case of degenerate polygonal mesh.

*Atomic Force Microscopy of DNA Nanostructures*: AFM of structures spread on mica was performed by preparing disc of mica fastened with epoxy adhesive to the center of a microscope slide and enclosed by a plastic ring attached with repro rubber. 10 µL of structures ($10 \times 10^{-9}$ M) suspended in TE-Mg buffer ($5 \times 10^{-3}$ M $MgCl_2$) were pipetted onto freshly cleaved mica for 30 s, at which point 4 µL of $5 \times 10^{-3}$ M NiSO4 (Merck Millipore) was added and incubated for 4.5 min, followed by rinsing the surface with 1 mL of TE-Mg buffer. 1.5 mL of TE-Mg buffer was added to the mica disk. Imaging was performed using a JPK instruments nanowizard 3 ultra with a Bruker Scanasyst fluid with cantilever in AC mode. Anchored structures were imaged on cover glass prepared according to the biotin BSA, streptavidin, and biotin-anchored structure incubation protocol described for DNA PAINT above in an spread dish and imaged in PBS with QI mode.

*Dynamic Light Scattering and Zeta Potential Measurement*: DLS size measurements were performed using a Zetasizer Nano ZSP (Malvern Instruments) equipped with a 633 nm He-Ne laser, at 25 °C, at 173° scattering angle, in ZEN0040 disposable cuvettes, with 25 measurements per replicate, and three experimental replicates per condition. Dispersants were filtered prior to the introduction of particles to remove dust and other particulate contaminants using a 0.22 µm cut-off cellulose syringe filter. Distribution analysis was performed using the Zetasizer software, with the CONTIN algorithm used to extract peaks from the heterogeneous/polydisperse samples. A screen for appropriate concentrations was performed independently for BSA and structures respectively, with 10 and $1 \times 10^{-9}$ M being the final concentrations used for data collection. Zeta potential measurements were performed using the Zetasizer Nano ZSP. Measurements were taken at 25 °C in disposable DTS1070 electrophoresis cuvettes, with between 10 and 50 measurements per sample and triplicate samples. The dispersion media used for DLS and zeta potential were either PAINT buffer B ($5 \times 10^{-3}$ M tris, $10 \times 10^{-3}$ M MgCl2, $1 \times 10^{-3}$ M EDTA, 0.05% TWEEN, pH 8) or variants of blood plasma mimicking buffer (Table S1, Supporting Information), and dispersion medium parameters (viscosity and refractive index) used were estimated on the basis of their constituent components and are shown in Table S2 of the Supporting Information. The particle refractive indices used were 1.460 for DNA nanostructures and 1.450 for BSA.

*Coarse Grained Simulation of DNA Nanostructures*: Structures were simulated using oxDNA's molecular dynamics algorithm.[32–35] Each design was simulated for $10^9$ timesteps, with each timestep size 0.005 oxDNA time units, or $3.03 \times 10^{-12}$ s, referred to as the time factor, and thus a total simulation time of 15.15 µs. Anchored structures work by trapping one particle with a force directing the particle always to a fixed initial position. A repulsion field was also introduced below anchored structures to prevent nucleotides from entering one half of the total possible volume. The salt concentration parameter was set to $163 \times 10^{-3}$ M, corresponding to the net monovalent cation concentration of PBS. Simulations were run at 30 °C with a Brownian (John) thermostat responsible for updating nucleotide momenta with a probability determined by the diffusion coefficient (2.5 in simulation length units (1 unit = 0.8518 nm). A large bounding box was utilized to avoid boundary effects ($400 \times 400 \times 400$ in oxDNA length units). Simulations were run in parallel on GPUs. Simulation parameters are summarized in Table S3 of the Supporting Information along with further discussion of simulation approach and the extraction of radial data. Results of simulation trajectories for hexagonal, octagonal, and rectangular nanostructure variants are shown in Figures S6 and S7 of the Supporting Information. Radial measurement of simulated structures is depicted in Figure S10 of the Supporting Information.

## Supporting Information

Supporting Information is available from the Wiley Online Library or from the author.

## Acknowledgements

The authors would like to thank M. Carroni for assistance with cryo-EM.

## Conflict of Interest

The authors declare no conflict of interest.

## Keywords

DNA nanostructures, DNA nanotechnology, DNA origami, molecular machines, superresolution microscopy

Received: September 4, 2018
Revised: November 19, 2018
Published online:

[1] J. Chen, N. C. Seeman, *Nature* **1991**, *350*, 631.
[2] P. W. K. Rothemund, *Nature* **2006**, *440*, 297.
[3] D. Han, S. Pal, J. Nangreave, Z. Deng, Y. Liu, H. Yan, *Science* **2011**, *332*, 342.
[4] S. M. Douglas, H. Dietz, T. Liedl, B. Högberg, F. Graf, W. M. Shih, *Nature* **2009**, *459*, 414.
[5] B. Högberg, T. Liedl, W. M. Shih, *J. Am. Chem. Soc.* **2009**, *131*, 9154.
[6] T. Liedl, B. Högberg, J. Tytell, D. E. Ingber, W. M. Shih, *Nat. Nanotechnol.* **2010**, *5*, 520.
[7] E. Benson, A. Mohammed, J. Gardell, S. Masich, E. Czeizler, P. Orponen, B. Högberg, *Nature* **2015**, *523*, 441.
[8] H. Dietz, S. M. Douglas, W. M. Shih, *Science* **2009**, *325*, 725.
[9] P. Yin, H. Yan, X. G. Daniell, A. J. Turberfield, J. H. Reif, *Angew. Chem., Int. Ed.* **2004**, *43*, 4906.
[10] Y. Suzuki, M. Endo, Y. Katsuda, K. Ou, K. Hidaka, H. Sugiyama, *J. Am. Chem. Soc.* **2014**, *136*, 211.
[11] N. V. Voigt, T. Tørring, A. Rotaru, M. F. Jacobsen, J. B. Ravnsbæk, R. Subramani, W. Mamdouh, J. Kjems, A. Mokhir, F. Besenbacher, K. V. Gothelf, *Nat. Nanotechnol.* **2010**, *5*, 200.
[12] M. De Stefano, K. Vesterager Gothelf, *ChemBioChem* **2016**, *17*, 1122.
[13] R. Veneziano, S. Ratanalert, K. Zhang, F. Zhang, H. Yan, W. Chiu, M. Bathe, *Science* **2016**, *352*, 1534.
[14] J. Nangreave, H. Yan, Y. Liu, *J. Am. Chem. Soc.* **2011**, *133*, 4490.
[15] D. Y. Zhang, A. J. Turberfield, B. Yurke, E. Winfree, *Science* **2007**, *318*, 1121.
[16] A. E. Marras, L. Zhou, V. Kolliopoulos, H. J. Su, C. E. Castro, *New J. Phys.* **2016**, *18*, 055005.
[17] A. E. Marras, L. Zhou, H.-J. Su, C. E. Castro, *Proc. Natl. Acad. Sci. USA* **2015**, *112*, 713.
[18] B. Saccà, Y. Ishitsuka, R. Meyer, A. Sprengel, E. C. Schöneweiß, G. U. Nienhaus, C. M. Niemeyer, *Angew. Chem., Int. Ed.* **2015**, *54*, 3592.
[19] T. Gerling, K. F. Wagenbauer, A. M. Neuner, H. Dietz, *Science* **2015**, *347*, 1446.
[20] K. Lund, A. J. Manzo, N. Dabby, N. Michelotti, A. Johnson-Buck, J. Nangreave, S. Taylor, R. Pei, M. N. Stojanovic, N. G. Walter, E. Winfree, H. Yan, *Nature* **2010**, *465*, 206.
[21] E. S. Andersen, M. Dong, M. M. Nielsen, K. Jahn, R. Subramani, W. Mamdouh, M. M. Golas, B. Sander, H. Stark, C. L. P. Oliveira, J. S. Pedersen, V. Birkedal, F. Besenbacher, K. V. Gothelf, J. Kjems, *Nature* **2009**, *459*, 73.

[22] R. P. Goodman, M. Heilemann, S. Doose, C. M. Erben, A. N. Kapanidis, A. J. Turberfield, *Nat. Nanotechnol.* **2008**, *3*, 93.
[23] Y. Krishnan, F. C. Simmel, *Angew. Chem., Int. Ed.* **2011**, *50*, 3124.
[24] E. Benson, A. Mohammed, A. Bosco, A. I. Teixeira, P. Orponen, B. Högberg, *Angew. Chem., Int. Ed.* **2016**, *55*, 8869.
[25] E. Benson, A. Mohammed, D. Rayneau-Kirkhope, A. Gådin, P. Orponen, B. Högberg, *ACS nano* **2018**, *12*, 9291.
[26] R. Jungmann, M. S. Avendaño, J. B. Woehrstein, M. Dai, W. M. Shih, P. Yin, *Nat. Methods* **2014**, *11*, 313.
[27] J. Schnitzbauer, M. T. Strauss, T. Schlichthaerle, F. Schueder, R. Jungmann, *Nat. Protoc.* **2017**, *12*, 1198.
[28] N. Fogh-Andersen, *Clin. Chem.* **1977**, *23*, 2122.
[29] H. S. Antila, M. Sammalkorpi, *J. Phys. Chem. B* **2014**, *118*, 3226.
[30] R. Jungmann, C. Steinhauer, M. Scheible, A. Kuzyk, P. Tinnefeld, F. C. Simmel, *Nano Lett.* **2010**, *10*, 4756.
[31] C. E. Aitken, R. A. Marshall, J. D. Puglisi, *Biophys. J.* **2008**, *94*, 1826.
[32] T. E. Ouldridge, A. A. Louis, J. P. K. Doye, *J. Chem. Phys.* **2011**, *134*, 085101.
[33] T. E. Ouldridge, A. A. Louis, J. P. K. Doye, *Phys. Rev. Lett.* **2010**, *104*, 178101.
[34] J. P. K. Doye, T. E. Ouldridge, A. A. Louis, F. Romano, P. Šulc, C. Matek, B. E. K. Snodin, L. Rovigatti, J. S. Schreck, R. M. Harrison, W. P. J. Smith, *Phys. Chem. Chem. Phys.* **2013**, *15*, 20395.
[35] B. E. K. Snodin, F. Romano, L. Rovigatti, T. E. Ouldridge, A. A. Louis, J. P. K. Doye, *ACS Nano* **2016**, *10*, 1724.

 